aerospace

MDPI

Article

Advanced Sensor Tasking Strategies for Space Object Cataloging

Alessandro Mignocchi *, Sebastian Samuele Rizzuto, Alessia De Riz and Marco Felice Montaruli

Department of Aerospace Science and Technology, Politecnico di Milano, Via La Masa 34, 20156 Milan, Italy; sebastiansamuele.rizzuto@polimi.it (S.S.R.); alessia.deriz@polimi.it (A.D.R.); marcofelice.montaruli@polimi.it (M.F.M.)

* Correspondence: alessandro.mignocchi@polimi.it

Abstract

Space Surveillance and Tracking (SST) plays a crucial role in ensuring space safety. To this end, accurate and numerous observational resources are needed to build and maintain a catalog of space objects. In particular, it is essential to develop optimal observation strategies to maximize both the number and the quality of detections obtained from a sensor network. This represents a key step in the assessment of the network through simulations. This work presents the integrated development of sensor tasking strategies for optical systems and a track-to-track correlation pipeline within SΞNSIT, a software environment designed to simulate sensor network configurations and evaluate cataloging performance. For high-altitude low Earth orbit (HLEO) targets, which are fast-moving and widely distributed, tasking strategies emphasize systematic scans of the Earth's shadow boundary to exploit favorable phase angles and improve observational accuracy, while medium- and geostationary-Earth orbits (MEO–GEO) rely on equatorial-plane scans. The correlation pipeline employs Two-Body Integrals, uncertainty propagation, and a χ^2-test with the Squared Mahalanobis Distance to associate tracks and perform initial orbit determination of newly detected objects. Results indicate that the integrated approach significantly enhances detection coverage, leading to greater catalog build-up efficiency and improved SST performance. Consequently, it facilitates the cataloging of numerous uncataloged objects within a reduced timeframe.

Keywords: space situational awareness; space surveillance and tracking; space traffic management; resident space objects; observation strategies; optical sensors; track-to-track; orbit determination; cataloging; SΞNSIT

Check for updates

Academic Editor: Gang Zhang

Received: 19 November 2025
Revised: 5 January 2026
Accepted: 8 January 2026
Published: 12 January 2026

Copyright: © 2026 by the authors. Licensee MDPI, Basel, Switzerland. This article is an open access article distributed under the terms and conditions of the Creative Commons Attribution (CC BY) license.

1. Introduction

In recent years, the number of objects orbiting the Earth has increased exponentially, with Resident Space Objects (RSOs) posing significant challenges to space agencies, institutions, and private companies worldwide [1]. Since the beginning of space activities, approximately 23,770 satellites have been placed into Earth orbit through about 6990 rocket launches. In addition, more than 650 break-ups, explosions, collisions, and other anomalous fragmentation events have been recorded, further contributing to orbital congestion [2]. As a result, current estimates indicate the presence of nearly 54,000 space objects larger than 10 cm (including about 9300 active payloads), along with statistical models predicting about 1.2 million debris objects between 1 cm and 10 cm in size, and roughly 130 million between 1 mm and 1 cm. Within this increasingly congested environment, more than 42,830 RSOs are regularly tracked by space surveillance networks and maintained in their catalogs, requiring continuous monitoring and optimization of observational resources.

As the orbital environment becomes increasingly complex, the probability of conjunctions between operational spacecraft and fragments or between spacecraft themselves rises markedly, imposing substantial collision avoidance requirements on satellite operators. Moreover, uncontrolled re-entries of large debris pose non-negligible risks to terrestrial assets and populations [3], elevating the necessity for precise orbital monitoring and timely conjunction assessment [4]. This complexity transcends any single orbital regime: Low Earth Orbit (LEO), Medium Earth Orbit (MEO), and Geostationary Orbit (GEO) all exhibit exponential growth in cataloged objects, driven by both intentional constellations and accidental fragmentation events.

In this context, several national and international Space Surveillance and Tracking (SST) initiatives have been developed, including the United States Space Surveillance Network (USSSN) [5], the European Space Agency (ESA) Space Situational Awareness (SSA) program [6], and the European Union's Space Surveillance and Tracking (EUSST) framework [7]. The latter brings together national agencies and institutions from 15 EU member states and is responsible for providing services such as collision avoidance [8,9], fragmentation analysis [10,11], and re-entry [12–14].

SST operations are fundamental to the safe and sustainable use of Earth's orbits, as they provide continuous situational awareness of RSOs [15]. The services provided rely on the space object catalog, which is maintained through orbit determination procedures [16] based on measurements collected by ground- and space-based sensors, such as optical [17–19], laser [20,21], and radar [22–24] systems. Radar sensors are predominantly employed for tracking RSOs in LEO, since the power of the received signal decreases with the increasing of the target distance. Optical systems are typically employed for LEO, MEO, and GEO, and they are advantageous when transit predictions are available, which enables refined orbit determination (ROD) [25,26] and improves the accuracy of cataloged objects. Conversely, when no prior orbital knowledge exists, measurements acquired are exploited to characterize an object orbital state, enabling initial orbit determination (IOD) [27–30]. This process is particularly important for reconstructing the orbits of fragments produced by in-orbit breakups and for tracking satellites in the final phases of reentry, where environmental perturbations quickly degrade prediction reliability. However, due to the vast number of RSOs requiring tracking, detection, and re-observation, ground- and space-based sensors collectively strive to maintain a comprehensive catalog, yet finite observational resources and competing priority tasks frequently result in coverage gaps [31]. Consequently, optimizing the end-to-end cataloging pipeline, from detection to orbit determination and update, becomes essential to maximize the utility of existing sensor networks and to ensure persistent surveillance.

To address these challenges, different survey strategies are proposed and tested in literature to optimize the observational resource available in a space surveillance network. Within the framework of the EUSST, the COPLA (Coordinated Planner) tool [32] introduces a centralized survey strategy designed to optimize the use of heterogeneous sensors across the network. Its survey chain focuses on optical sensors and selects declination bands and right ascension regions based on orbital parameters and object concentration, while accounting for observational constraints such as the Moon, the galactic plane, and the Earth's shadow. The strategy aims to maximize effective surveillance time and improve the brightness conditions of observed objects, thereby enhancing orbit covariance accuracy. These improvements are subsequently fed into the tracking chain to refine tasking requests and catalog maintenance, ultimately ensuring a more efficient allocation of limited observational resources and a higher quality of the space object catalog. Another approach to sensor tasking for SSA has emphasized survey strategies that balance catalog build-up with orbit determination accuracy. Schubert et al. [33] propose a stripe-scanning approach for tele-

scopes in GEO surveys, complemented by greedy optimization for follow-up tasks. The vertical and horizontal stripe-scanning methods enable repeated observations of objects along different orbital positions within a single night, improving the probability of successful IOD with angles-only data. Horizontal scanning, in particular, yields higher unique detections and more accurate ephemerides compared to untasked or fixed-line-of-sight strategies. Beyond optical surveys, recent studies have explored global radar network tasking for LEO domain awareness, emphasizing the need for worldwide coordination to maintain persistent tracking [34]. In this context, Rowland et al. demonstrated that the collective performance of a distributed phased-array infrastructure significantly enhances catalog maintenance compared to standalone assets. Their analysis highlighted that maximizing network-level metrics, such as median revisit time and search completeness, requires strategic geographic distribution to ensure robust coverage across all orbital inclinations.

However, a significant research gap persists in the development of multi-regime strategies capable of simultaneously managing the distinct dynamical and photometric constraints of LEO, MEO, and GEO populations. Current methodologies are predominantly regime-specific—employing techniques such as stripe-scanning or declination bands—and inherently fail to address the heterogeneous nature of the global space environment. Furthermore, existing approaches typically isolate catalog build-up from follow-up optimization, lacking a cohesive architecture that integrates both objectives. Computational challenges also remain unresolved: heuristic optimizations, such as greedy or genetic algorithms, are prone to local minima and high processing costs, while established survey chains like COPLA frequently rely on static assumptions regarding orbital distributions and illumination. These limitations collectively result in persistent coverage gaps, suboptimal revisit rates, and reduced adaptability to dynamic observation conditions.

To overcome these research gaps, this work introduces a scientific and technological advancement in SST simulation by upgrading the SΞNSIT framework [35] with a dedicated observation strategy designed for multi-regime monitoring. The originality of this contribution lies in the development of a unified observation plan that integrates a phase-aware fence and an equatorial fence to provide simultaneous coverage across HLEO, MEO, and GEO. Specifically, the phase-aware strategy dynamically scans the Earth's shadow boundary to exploit favorable phase angles, thereby maximizing the Signal-to-Noise Ratio (SNR) and improving the detection of faint objects in HLEO—a capability lacking in conventional static approaches. Complementary to this, the equatorial fence ensures persistent surveillance of higher-altitude populations. This integrated approach enables the detection of heterogeneous orbital populations within a single nightly campaign, significantly reducing coverage gaps and enhancing the overall fidelity of the simulated SST network. Furthermore, system performance is evaluated by incorporating the first stage of objects cataloging: data generated by the survey strategy are processed through a track-to-track association module, which links observed tracks and enables the estimation of target orbits. The performance of the orbit estimation algorithms is assessed across HLEO, MEO, and GEO regimes, demonstrating the framework capability to support accurate cataloging in a multi-regime monitoring context.

The remainder of this paper is structured as follows: Section 2 presents SΞNSIT. Section 3 details the software upgrades, including an in-depth description of the newly developed observation strategy (Section 3.1) and the track-to-track association and IOD algorithms (Section 3.2). Section 4 describes the simulation campaign used to evaluate these novel methodologies, and Section 5 offers concluding remarks.

2. SΞNSIT

SΞNSIT [35] is a comprehensive end-to-end software environment for the simulation and assessment of SST architectures. It has been developed by the Department of Aerospace Science and Technology (DAER) at Politecnico di Milano. Written in Python 3 and C++, the tool is designed to run on Windows, macOS, and Linux, and relies on the NASA/NAIF SPICE library [36] to ensure precise astronomical and geometrical computations. Configuration is managed via YAML files, and all simulation data are internally stored in an SQLite database. Interaction can be achieved either through a command-line interface for automation and scripting or via a Qt-based graphical interface for user-friendly configuration and visualization.

SΞNSIT is conceived as a modular and flexible framework able to reproduce the behavior of heterogeneous SST networks, supporting both ground-based and space-based assets, including optical telescopes and radar stations. Its architecture allows users to evaluate the performance of different network configurations with respect to coverage, detection efficiency, catalog build-up, and long-term catalog maintenance. The tool also supports sensitivity analyses to assess the robustness of a given network under varying assumptions, such as sensor placement, scheduling policies, and orbital population characteristics. This makes SΞNSIT particularly suited to both research applications and decision-making processes for operational SST architectures.

A key strength of the software lies in its ability to reproduce the entire surveillance chain: given a defined reference population of RSOs, a network of ground and/or space sensors, and a time window of interest, SΞNSIT computes observable passes, generates optimized survey and tracking schedules according to user-defined criteria, simulates realistic acquisitions with configurable sensor accuracies and propagates the results into catalog build-up and maintenance processes. This integrated approach makes it possible to test novel observation strategies and tasking algorithms within a controlled simulation environment before their potential adoption in real SST operations.

As illustrated in Figure 1, the software is organized into six main modules:

- Data initialization: Handles preprocessing of input data, updates SPICE kernels for planetary ephemerides and leap seconds, and initializes the simulation environment. In particular, this module manages orbit propagation by generating SPK Type 10 kernels from the input Two-Line Elements (TLEs), allowing the software to compute state vectors via the SGP4 analytical propagator [37].
- Survey strategy definition: Computes pointing sequences as a function of time and angular coordinates, implementing observation strategies tailored to different sensor types (e.g., optical and radar) and orbital regimes.
- Pass computation: Evaluates observable passes for all objects of interest, accounting for a wide range of observability limits including geometric constraints (e.g., elevation), Field-of-View (FoV) pointing (defined through the observation strategy module for survey sensors), physical limitations, illumination conditions, minimum Sun/Moon/Earth separation angles, and maximum signal loss or apparent magnitude thresholds [38].
- Observation scheduling: Employs a genetic algorithm [39,40] to optimize the selection of passes, balancing coverage, revisit times, and resource allocation for tracking tasks.
- Catalog build-up/maintenance: Simulates sensor measurements, performs orbit determination and track-to-track correlation, and updates the catalog iteratively to mimic real surveillance operations.
- Performance analysis: Generates statistical and graphical outputs, enabling comparisons across strategies and architectures through metrics such as coverage, detection rates, catalog accuracy, and computational costs.

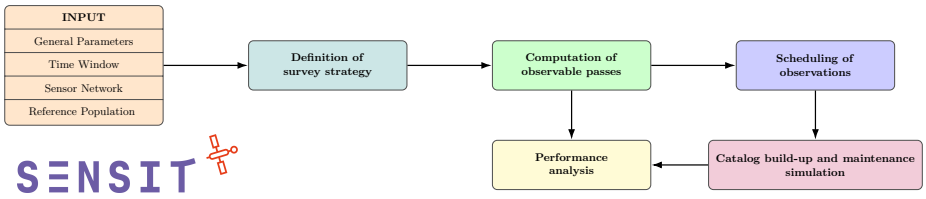

Figure 1. Block diagram of the SΞNSIT software architecture, showing the end-to-end pipeline from user-provided inputs (general parameters, time window, sensor network configuration, and reference population) through survey strategy definition, observable pass computation, observation scheduling, catalog build-up and maintenance simulation, and concluding with performance analysis.

To ensure simulation fidelity, SΞNSIT models the physical limitations of the observing sites and sensors. For optical sensors, the framework verifies Sun illumination of the object and accounts for atmospheric extinction based on station altitude and target elevation. Environmental conditions are further integrated through the estimation of background sky brightness and SNR thresholds, while radar sensors are evaluated against signal loss and Radar Cross Section (RCS) filters. Additionally, the tool enforces operational constraints such as minimum pass lengths and maximum subpass durations to prevent sensor saturation.

This study presents the newly developed implementation of SΞNSIT, with particular emphasis on the survey strategy module introduced herein, and the correlation pipeline, which plays a key role in catalog construction and maintenance, as detailed in Section 3.

3. Methodology and Software Upgrades

In this work, SΞNSIT has been extended to broaden its simulation capabilities, thus producing a more advanced and accurate tool for assessing both SST network performance and catalog fidelity. The survey strategy module was incorporated to enable the simulation of sensor pointing sequences instead of the fixed-point survey and tracking modes that characterized the previous software release. Furthermore, as detailed in Section 3.1, a novel observation strategy was developed and integrated to enhance the contribution and efficiency of optical sensors in monitoring large populations of RSOs across multiple orbital regimes, along with the introduction of an SNR check to ensure the reliability of the observed detections. Moreover, Section 3.2 introduces the new track-to-track pipeline within the catalog build-up and maintenance module.

3.1. Observation Strategy

This work introduces a novel multi-regime observation strategy within SΞNSIT, representing a significant technological advancement over previous survey modes. The originality of this approach lies in the integration of two complementary, dynamically adapting scanning modes [41], each scientifically optimized to enhance both coverage and measurement fidelity across heterogeneous orbital populations:

- Phase-aware fence: Unlike conventional fixed-pointing strategies, this mode provides an advanced scientific improvement by continuously scanning the marginally illuminated boundary of Earth's shadow cone. This optimization of the phase angle for HLEO targets directly improves the SNR, enabling the detection of faint objects with higher-precision angular and photometric measurements [42].
- Equatorial fence: Operating in tandem with the phase-aware mode, this strategy provides comprehensive surveillance of the celestial band where RSOs intersect the Earth's equatorial plane. This ensures a unified observation plan capable of covering both MEO and GEO populations with high temporal revisit rates: a technological capability not achievable with single-regime survey methods.

3.1.1. Shadow Cone Modeling

The phase-aware fence mode is activated only when the conical section of Earth's shadow, specified by a fixed user-defined altitude, is at least partially visible from the observing station, subject to the relevant line-of-sight and geometric constraints. To determine the instantaneous position of the shadow boundary, the umbra is modeled using the Spherical Earth Conical Shadow Model (SECSM) [43,44], which represents the Earth's shadow as a right circular cone extending into space. This conical representation permits real-time computation of the shadow boundary coordinates, from which the appropriate sensor pointing sequence is derived and continuously updated to maintain optimal phase angles for measurements.

Assuming the Earth to be spherical, the shadow cast by the Sun forms a conical projection consisting of two regions: the umbra and the penumbra. Within the scope of this work, only the umbra is considered. The resulting umbral cone model is described based on the Earth-Sun geometry illustrated in Figure 2.

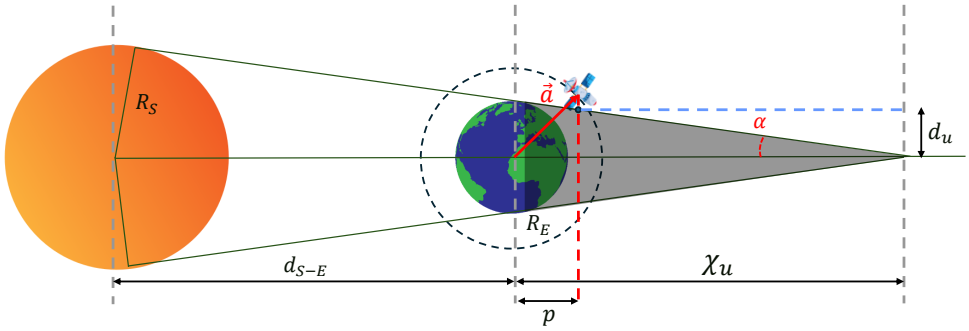

Figure 2. Earth-Sun geometry and spherical Earth conical shadow model. The Sun (R_S) and Earth (R_E) are separated by d_{S-E}. Tangents define the umbral cone of length χ_u and diameter d_u. A satellite at position $\vec{a}$ lies outside the shadow cone, with p the projection distance and α the half-cone angle [43].

Let the vectors $\vec{a}$ and $\vec{d}_{S-E}$ denote the spacecraft and the Sun position vectors with respect to the geocenter, in the Earth Centered Intertial (ECI) reference frame. The projection vector $\vec{p}$ of vector $\vec{a}$ onto the Sun direction $\hat{d}_{S-E}$ is given by

$$\vec{p} = (\vec{a} \cdot \hat{d}_{S-E})\, \hat{d}_{S-E}. \tag{1}$$

As discussed by Srivastava et al. [45], the spacecraft may enter the Earth's shadow only if the condition $\vec{a} \cdot \hat{d}_{S-E} < 0$ is satisfied.

To determine the ECI position of the Earth's shadow cone boundary at a given altitude, it is first necessary to establish the geometric parameters that define the cone in space. Let X_u denote the distance between the umbral cone vertex and the Earth's center, α the semi-aperture angle of the umbral cone, and d_u the distance from the cone axis to the umbral terminator point at the projected spacecraft location along the Earth-Sun axis. From the umbral cone geometry [46], the following relations are obtained:

$$\begin{cases} X_u = \dfrac{R_E\, d_{S-E}}{R_S - R_E} \\ \alpha = \sin^{-1}\left(\dfrac{R_S - R_E}{d_{S-E}}\right) \\ d_u = (X_u - p)\tan(\alpha) \end{cases} \tag{2}$$

Once these geometrical quantities are determined, the complete three-dimensional shape of the Earth's shadow in space can be defined. For this work, the objective is to characterize the shadow cone boundary in the ECI reference frame, in order to determine the illumination conditions at the inertial positions of the RSOs. This boundary is obtained as a conical section of the modeled shadow cone, resulting from the intersection of the cone with a sphere at a specific reference altitude above the Earth's surface. In a subsequent step, the coordinates are converted into the topocentric reference frame to determine the pointing sequence angles tailored for the specific sensor. Since the implemented phase-aware strategy is designed for HLEO objects, the boundary is set by default at an altitude of 1000 km, corresponding to the intersection of the cone with a sphere of radius $R_E + h_{HLEO}$, where h_{HLEO} denotes the reference minimum altitude of HLEO objects [47], as illustrated in Figure 3.

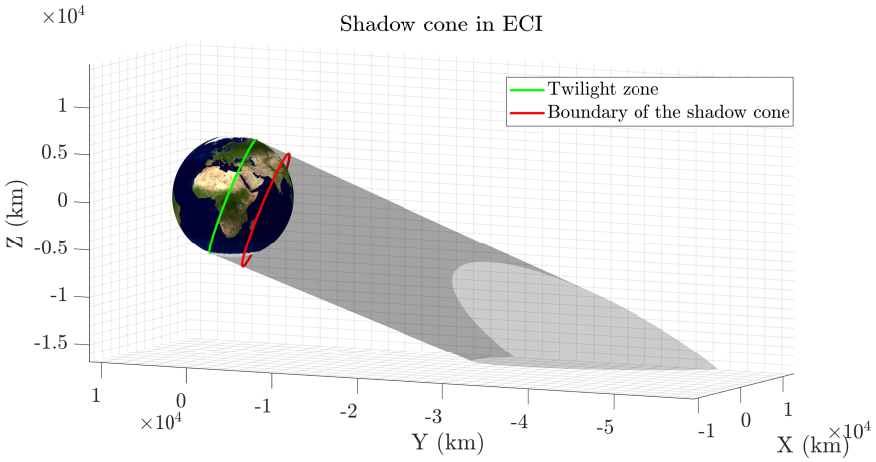

Figure 3. Earth's shadow cone in the ECI J2000 frame. The green curve marks the terminator-the boundary between Earth's day side and night side-while the red curves trace the edges of the shadow cone at an altitude of 1000 km.

3.1.2. Pointing Sequence Strategy

A key technological contribution of this module is the implementation of a continuous dynamical updating algorithm for the sensor pointing sequence. Constructing a scanning sequence that follows the shadow cone boundary demands continuous recalculation, as Earth's rotation causes the cone to shift rapidly inside sensors topocentric frame. This work addresses the challenge of inadvertent pointing into shaded regions by re-computing the shadow edge after each full scansion. This approach strikes an effective balance between computational efficiency and the need for a near-continuous, dynamically accurate pointing sequence that remains illuminated throughout the scan.

Furthermore, determining the physically optimal pointing sequence is complicated by the fact that the Sun's shadow cone boundary changes shape within the topocentric reference frame. As a result, the illuminated portion of this boundary does not necessarily correspond to the exterior region of the curve projected onto the topocentric sphere. Specifically, the intersection between the circular cross-section of the shadow cone and the hemispherical representation of the sky can alter the resulting dark region. As a result, the observation strategy may, in certain cases, require redirecting the sensor toward the inner segment of the curve that delineates the sunlit portion of the sky. Figure 4 presents a single complete scan of the visible portion of the shadow cone, depicted in both planar and three-dimensional views.

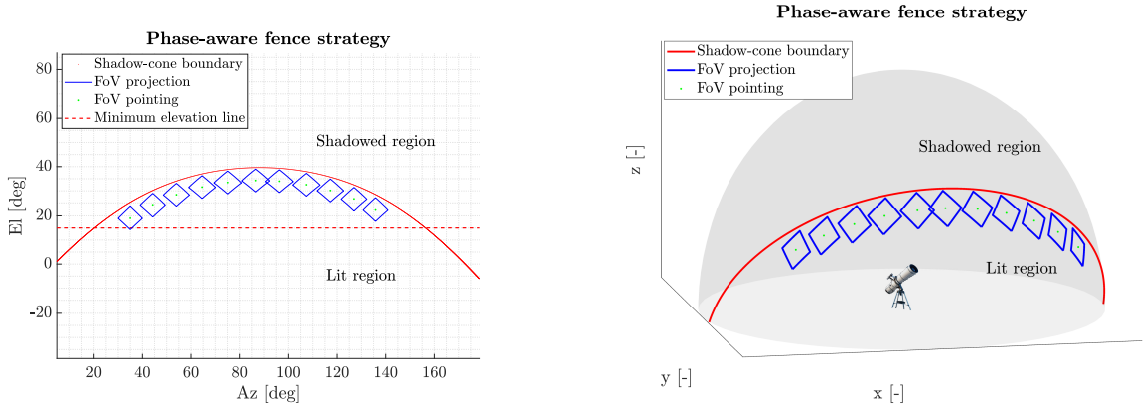

(**a**) 2D topocentric representation. (**b**) 3D topocentric representation.

Figure 4. Representation of one full phase-aware fence scansion of the shadow cone boundary in the 2D topocentric reference frame (**a**) and in the 3D topocentric reference frame (**b**).

On the other hand, the equatorial fence strategy is delivered whenever the observing station is in local darkness and the Earth's shadow cone is not visible, thereby providing complementary coverage across orbital regimes. In this mode, the Earth's equatorial plane is projected at a user-defined altitude, typically between 2000 km and 35,786 km to encompass both MEO and GEO populations [48], and is scanned in a serpentine pattern (Figure 5) to capture objects as they cross the equatorial plane. Since the equatorial projection exhibits minimal apparent motion during a single scan, the initial pointing sequence remains valid throughout. However, the projection is deterministically recalculated after each complete scan to maintain pointing accuracy and enhance revisit rates.

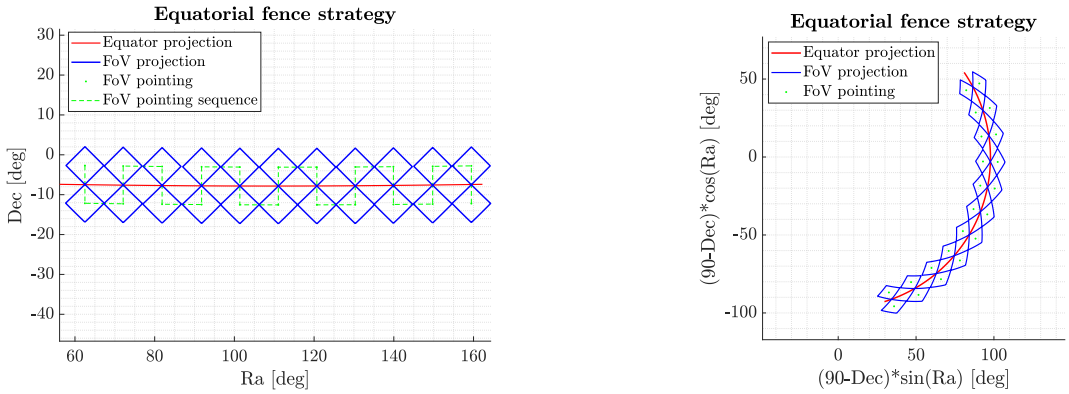

(**a**) Equatorial representation. (**b**) Polar projection representation.

Figure 5. Representation of one full equatorial fence scansion of the equator projection in the equatorial coordinate system (Right Ascension and Declination) centered in the station (**a**) and the related polar projection (**b**).

The selection of observation strategy parameters is driven by both dynamical and operational considerations, as it will be better outlined in Section 4.2. In particular, the exposure time is adjusted according to the apparent angular velocity of the objects in the topocentric reference frame. Targets observed in low-altitude regions, such as those within the phase-aware fence, exhibit higher apparent motion across the field of view, thus requiring shorter exposure times to limit image trailing and preserve both SNR and astrometric accuracy. Conversely, objects at higher altitudes, as in the equatorial fence, move more slowly and allow for longer exposures. The readout time is kept constant, being primarily dictated by sensor characteristics and not significantly affecting the survey cadence optimization.

Finally, the number of acquisitions per field of view is chosen to ensure a sufficient set of detections for IOD, typically requiring at least three well-spaced observations to achieve robust orbital solutions while maintaining overall survey efficiency. This strategy has been specifically developed for optical sensors, which alone enable comprehensive coverage across diverse orbital regimes.

3.1.3. SNR Check

To ensure the reliability of the simulated observations, a dedicated SNR validation step is introduced within the SΞNSIT software.

The photometric model implemented for the simulated telescopes estimates the apparent visual magnitude M_v of a satellite by combining the diffusive and specular reflection components of its surface. Given the Sun's apparent magnitude $M_\odot = -26.74$, the target effective reflective area A, the satellite-sensor range ρ, and the phase angle ϕ between the Sun, satellite, and observer, the apparent magnitude is expressed as

$$M_v = M_\odot - 2.5 \log_{10}\left(\frac{\rho_{\text{diff}} F_{\text{diff}}(\phi) + \rho_{\text{spec}} F_{\text{spec}}(\phi)}{\rho^2} A \right), \tag{3}$$

where ρ_{diff} and ρ_{spec} denote the diffusive and specular reflection coefficients, respectively. The angular reflection functions are given by

$$F_{\text{diff}}(\phi) = \frac{2}{3\pi^2}[(\pi - \phi)\cos\phi + \sin\phi], \qquad F_{\text{spec}}(\phi) = \frac{1}{4\pi}. \tag{4}$$

In this work, the effective reflective area A is approximated as equal to the target RCS. This represents a necessary hypothesis due to the lack of detailed data for the large-scale reference population studied. However, it is important to note that the RCS and the optical cross-section are not physically identical, as they depend on different interaction mechanisms across distinct wavelengths. This assumption may introduce errors in the estimated magnitude M_v, as it neglects the specific orientation of the satellite surfaces and the wavelength-dependent reflectivity, particularly for objects with complex geometries or high specular components.

From the apparent magnitude, the expected SNR is derived using a parametric model calibrated on the simulated optical telescope characteristics. The pixel-level SNR is defined as

$$\text{SNR}_{\text{pix}} = \frac{\dfrac{c_1\, 10^{10-0.4M_v}\, t_{\text{exp}}}{N_{\text{trail}}}}{\sqrt{\left(\dfrac{c_1\, 10^{10-0.4M_v}}{N_{\text{trail}}} + c_2\, 10^{10-0.4M_{\text{sky}}} + c_3 \right) t_{\text{exp}} + c_4}}, \tag{5}$$

where t_{exp} is the exposure time, N_{trail} is the trail length in pixels, $M_{\text{sky}} = 19.5$ is the background sky magnitude, and c_1, c_2, c_3, c_4 are empirically determined constants. The total SNR along the trail is then obtained as

$$\text{SNR}_{\text{trail}} = \text{SNR}_{\text{pix}} \sqrt{N_{\text{trail}}}. \tag{6}$$

This combined photometric and SNR model allows the simulation to reject passes that would not be detected or would not yield sufficiently reliable detections, ensuring that only high-quality measurements contribute to the catalog build-up analysis.

3.2. Track-to-Track Association and IOD

To describe the state of a target object within an ECI reference frame, the following relationships are generally employed:

$$\begin{aligned} \vec{r} &= \vec{R}_s + \rho\,\vec{s}, \\ \vec{v} &= \vec{V}_s + \rho\,\dot{\vec{s}} + \dot{\rho}\,\vec{s}, \\ \vec{s} &= (\cos\alpha\cos\delta, \sin\alpha\cos\delta, \sin\delta), \end{aligned} \tag{7}$$

where $\vec{r}$ is the target position and $\vec{v}$ its velocity, while $\vec{R}_s$ and $\vec{V}_s$ correspond to the ground station position and velocity and $\vec{s}$ is the line-of-sight unit vector. However, angular information alone, in the form of Right Ascension (Ra, α) and Declination (Dec, δ) pairs, is not sufficient to solve the problem. To address this, a track compression technique is employed to extract additional information about the angular velocities $(\dot{\alpha}, \dot{\delta})$. The procedure selected for the case at hand involves a second-order regression, performed at the midpoint of the uncorrelated track, which allows all the information contained in the track to be condensed into a single point. The result is a vector that includes both the angular coordinates and their respective time derivatives, which is commonly referred to in the literature as an optical attributable [49] and is defined as

$$\mathcal{A} = (\alpha, \delta, \dot{\alpha}, \dot{\delta}) \in [-\pi, \pi) \times (-\pi/2, \pi/2) \times \mathbb{R}^2\,. \tag{8}$$

The Two-Body Integrals (TBI) [50–52] method is an IOD technique that aims to provide an initial estimate of the orbit associated with a pair of observational tracks, condensed into attributables, and to assess the likelihood that they originate from the same object.

Given the attributable $\mathcal{A}$, that is a four-dimensional vector, to compute a full orbit, formed by six parameters, the computation of two further quantities at the same time instant is needed [50]. The unknown quantities are the range (ρ) and range rate ($\dot{\rho}$) corresponding to the two attributables. However, by exploiting the problem structure, the number of unknowns can be reduced to only the two ranges, with the corresponding range rates expressed as functions of these last.

The TBI method assumes an ideal and unperturbed dynamical model. Under this assumption, the conserved quantities of the two-body problem, namely, the angular momentum vector $\vec{h}$, the Laplace-Lenz vector $\vec{L}$, and the orbital energy E, remain constant. The residuals of these quantities are exploited to build up a system of nonlinear scalar equations with the two range values as unknowns as done in [52]. Solving this system by setting the residuals to zero yields the values of ρ_1 and ρ_2, from which the corresponding $\dot{\rho}_1$ and $\dot{\rho}_2$ can be computed.

$$\begin{cases} q(\rho_1, \rho_2) = 0 \rightarrow \vec{h} = const \\ p(\rho_1, \rho_2) = 0 \rightarrow \vec{L} = const \\ f(\rho_1, \rho_2) = 0 \rightarrow E = const \end{cases} \quad , \; \rho_1, \rho_2 > 0. \tag{9}$$

An initial guess for the values of ρ_1 and ρ_2 is required to initialize the solver. This estimate is obtained through a preliminary application of Gauss' method [53], which uses the full track data along with the associated observation epochs. A schematic overview of the TBI method and the subsequent measurement correlation process is shown in Figure 6.

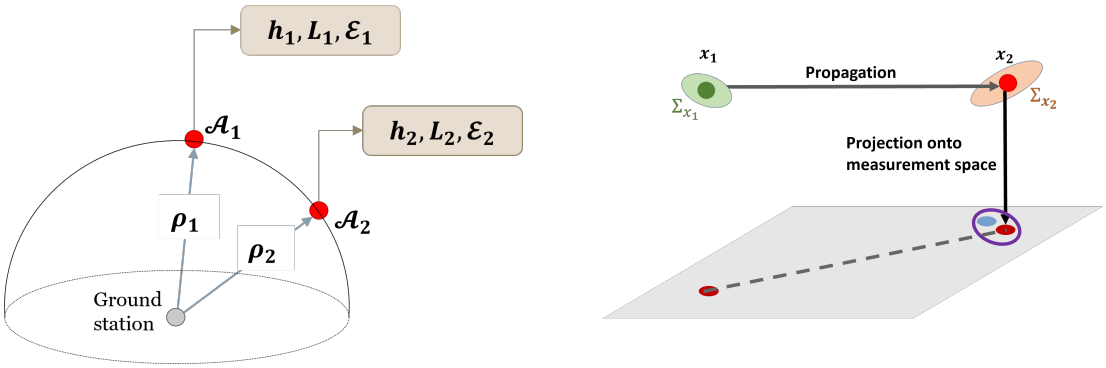

(**a**) TBI method. (**b**) Measurement correlation.

Figure 6. Visual representation of the TBI method (**a**) and the measurement correlation (**b**) steps.

Once the complete set of range and range-rate values is determined (ρ_1, ρ_2, $\dot{\rho}_1$, $\dot{\rho}_2$), the corresponding orbital states $\vec{x}_1(t_1)$ and $\vec{x}_2(t_2)$ can be reconstructed leveraging Equation (7). The state $\vec{x}_1(t_1)$ is then propagated using Keplerian dynamics to the epoch of the first observation, resulting in the orbit estimate $\vec{x}_{\text{IOD}}$. This output can be deterministic if no measurement uncertainty (mean and covariance) is provided, or stochastic. In the stochastic case, when the mean and covariance of the observations are available, the entire process is embedded within an Unscented Transform (UT), yielding the mean and covariance of $\vec{x}_{\text{IOD}}$.

It is necessary to clarify that the use of Keplerian dynamics within the IOD method introduces limitations that depend strongly on both the orbital regime and the time span separating the analyzed tracks. In general, the Keplerian assumption can be considered a reasonable approximation over time intervals that are short compared to the characteristic perturbation time scales of the object. Since the orbital period is not known a priori and may range from a few hours to approximately one day, the accuracy of the method varies accordingly. As a result, for a given time separation between tracks, superior performance is expected for objects exhibiting slower orbital dynamics compared to those with faster dynamics.

For correlation assessment, an initial check is performed on the covariance of $\vec{x}_{\text{IOD}}$ against predefined thresholds. Subsequently, the correlation hypothesis is verified by means of a Squared Mahalanobis Distance (SMD) based metric [54]. The estimated state distribution is propagated to the epochs of the observations within both tracks and projected onto the measurement space and compared against the actual angular measurements (α, δ) distribution via SMD. The SMD can be directly compared with a n-variable $\chi^2_{n,c}$ distribution quantifying its distance through a predefined confidence level c (related to a 3-σ factor distance from its mean), leading to the definition of the correlation index $corr_{idx} = \text{SMD}(x)/\chi^2_{n,c}$. Correlation is confirmed if $corr_{idx}$ falls below the threshold of 1.

4. Simulations and Results

This Section presents the simulation setup and corresponding results obtained using the SΞNSIT software. First, Section 4.1 describes the population of RSOs selected from the Space-Track catalog [55], including the altitude-based classification into HLEO, MEO, and GEO regimes. Next, Section 4.2 details the simulated ground-based sensor network, such as geographic locations, FoV, and visibility constraints, as well as the observation strategy settings. Section 4.3 reports the overall cataloging performance: Section 4.3.1 quantifies the number of detected passes per regime over a two-week time window, highlighting the

influence of orbital characteristics on detection efficiency, while Section 4.3.2 evaluates the track-to-track association performance of the proposed pipeline.

4.1. RSOs Population

The analysis draws on the Space-Track catalog [55]—a publicly accessible subset of the U.S. Space Surveillance Network maintained by the 18th Space Defense Squadron of USSPACECOM—by removing all objects that lack a valid RCS, have already decayed (re-entered Earth's atmosphere), or possess erroneous or incomplete TLEs data before further processing.

The resulting dataset contains 5096 objects spanning three orbital regimes: HLEO, MEO, and GEO. Each regime is defined by a specific altitude range, as summarized in Table 1. The majority of the RSOs in the dataset reside in the HLEO regime, followed by GEO and then MEO, reflecting the concentration of active satellites and debris in low- and high-altitude operational regions.

For the purpose of this work, and to compute the magnitude as in Equation (3), the geometric cross section was set equal to the RCS.

Table 1. Orbital regimes defined by altitude ranges and corresponding object counts after filtering.

Orbital Regime	Minimum Altitude	Maximum Altitude	Number of Objects
HLEO	1000 km	2000 km	3097
MEO	2000 km	33,786 km	575
GEO	33,786 km	37,786 km	1424
Total	–	–	5096

Figure 7 characterizes the filtered population in terms of its distribution across fundamental Keplerian parameters. Panel (**a**) maps object density in the semi-major axis–eccentricity (a–e) plane, highlighting the clear separation between the three orbital regimes. HLEO objects cluster at low altitudes with moderate eccentricities, while GEO objects appear as a dense band around $a \approx 42{,}164$ km. MEO objects populate the intermediate range, where characteristic eccentricities are generally low. Panel (**b**) shows the inclination-RAAN (i–Ω) distribution. The presence of distinct bands in inclination space reflects preferred orbital designs: near-zero inclinations for equatorial GEO satellites, high-inclination HLEO trajectories, and the 55–65° band associated with navigation constellations in MEO. The RAAN distribution appears nearly uniform, while distinct high-density clusters emerge at specific Ω values corresponding to operational constellation planes. A notable peak is observed around RAAN values of 80–100° combined with near-polar ($i \approx 90°$) orbits, which likely reflects the concentration of polar missions that preferentially occupy this region due to their favorable lighting and coverage conditions.

Figure 8 provides a complementary three-dimensional view of the dataset in the ECI J2000 reference frame. Here, the global spatial structure of the population becomes evident: the spherical HLEO shell surrounding Earth, the intermediate MEO band, and the concentrated GEO ring at the equatorial plane. Together, Figures 7 and 8 demonstrate the variety of the dataset, despite the filtering.

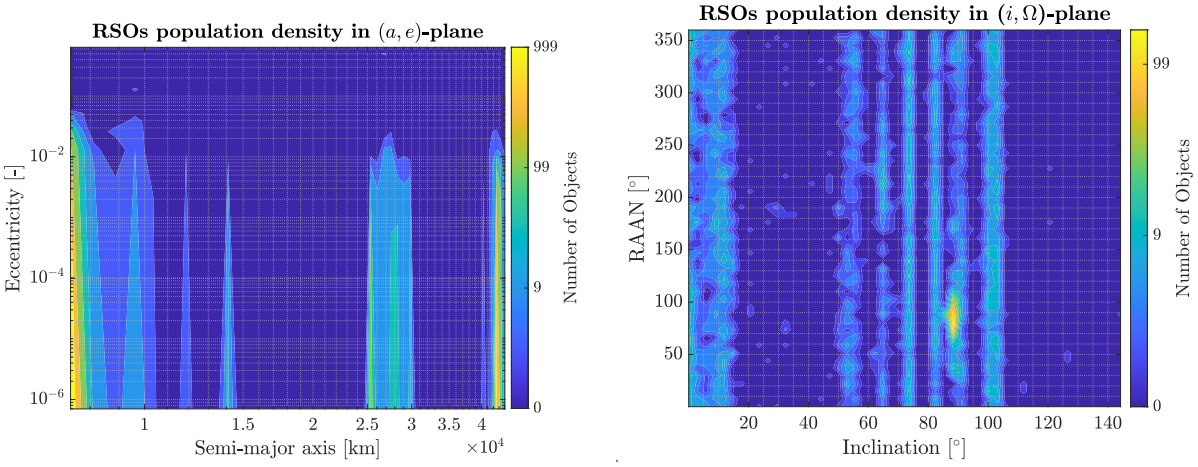

(**a**) Semi-major axis–eccentricity plane representation. (**b**) Inclination–RAAN plane representation.

Figure 7. Density distribution of simulated objects as a function of Keplerian orbital parameters: (**a**) variation of density with semi-major axis (a) and eccentricity (e); (**b**) variation of density with inclination (i) and right ascension of the ascending node (RAAN or Ω).

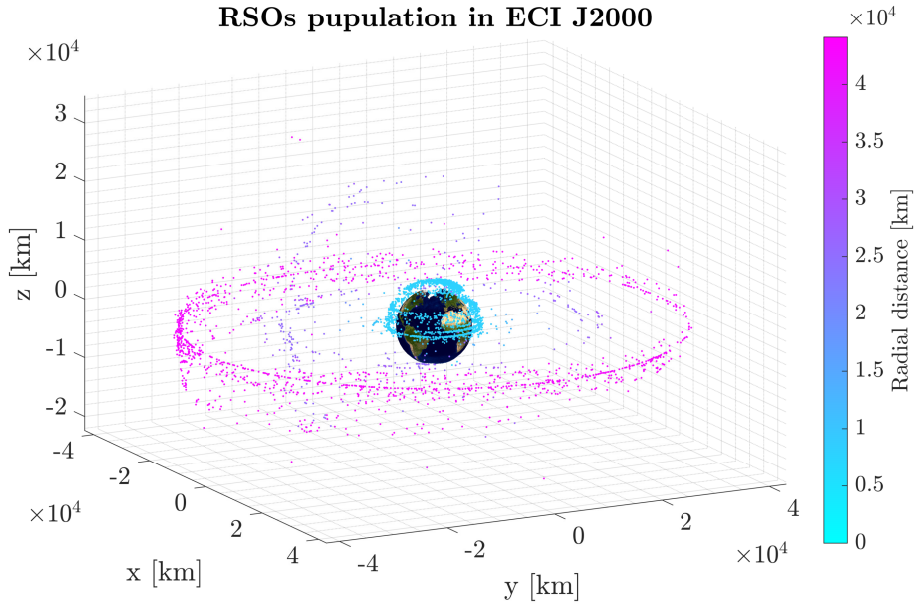

Figure 8. Distribution of simulated HLEO, MEO, and GEO objects in the ECI J2000 frame, sourced from Space-Track [55]. The colorbar represents the radial distance from Earth's center, with HLEO objects shown in light blue, MEO objects in shaded blue, and GEO objects in purple.

4.2. Sensor Network Definition

To assess the performance of the developed observation strategy, a global network of homogeneous optical sensors is simulated. Each sensor shares identical technical characteristics, while differing only in geographical location. The selected sites provide wide longitudinal coverage across both hemispheres, enabling near-continuous monitoring of RSOs across multiple orbital regimes.

The visibility constraints applied during the simulation include a minimum target elevation of 15° and a maximum Sun elevation of $-10°$ (to ensure the observation site is not illuminated by the sunlight). Additionally, any observation pass with a SNR below 6 is discarded (see Section 3.1.3). Each sensor is configured with a rectangular field of

view of 6.7° × 6.7°, aligned in right ascension and declination coordinates, and rotated by 45° counterclockwise.

The ground sensors are strategically positioned to provide both latitudinal and longitudinal diversity, as listed in Table 2. Stations such as Perdasdefogu, Teide, and La Silla cover Southern Europe and South America, while Tucson and Haleakala extend coverage over North America and the Pacific. Additional installations at New Norcia and Malargue enhance Southern Hemisphere visibility. This distribution reduces observational gaps caused by daylight and ensures that objects in geosynchronous, medium Earth, and low Earth orbits can be tracked over extended portions of their trajectories.

Table 2. Geographical distribution of the simulated optical sensors. The listed coordinates correspond to known optical-sensor or observatory installations whose approximate geographical positions are publicly available from open institutional sources or geospatial databases.

Station Location	Latitude [°]	Longitude [°]	Altitude [km]
Perdasdefogu	39.6614	9.4325	0.638
Tucson	31.9583	−111.5967	2.096
New Norcia	−31.0483	116.1919	0.252
Haleakala	20.7083	−156.2571	3.052
La Silla	−29.2612	−70.7313	2.332
Teide	28.3009	−16.5118	2.390
Malargue	−35.7733	−69.3997	1.400

The global spread of sensors also improves cataloging completeness by extending the available visibility windows. When one site becomes unavailable due to local constraints, another site at a different longitude can continue observations. Furthermore, the inclusion of stations at different latitudes improves the ability to detect objects in inclined orbits, thus ensuring broader coverage of the orbital population. Figure 9 shows the spatial distribution of the simulated network across the globe.

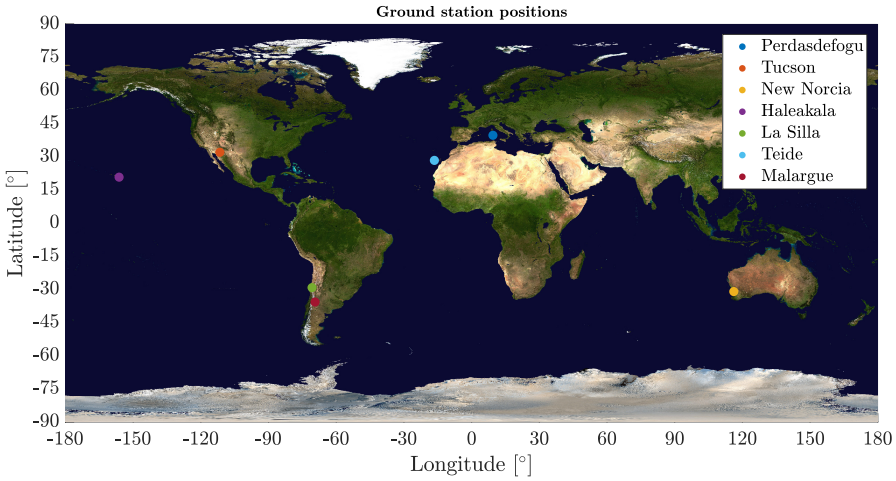

Figure 9. Geographical distribution of the ground-based sensor network simulated in this study. The wide longitudinal and latitudinal spread improves the coverage of different orbital regimes and extends visibility windows.

As introduced in Section 3, to define the observation strategy within SΞNSIT, additional optional parameters must be specified. The final observation strategy parameters employed in work are summarized in Table 3.

Table 3. Observation strategy settings employed within this work.

Parameter [u.o.m.]	Phase-Aware Fence	Equatorial Fence
Exposure time [s]	1.0	10.0
Readout time [s]	4.0	4.0
Projection altitude [km]	1000	28,000
Number of acquisitions per FoV [-]	3	3

4.3. Results

This section presents the main outcomes of the simulation campaign, including the detection performance achieved during the two-week optical observations and the subsequent track-to-track correlation analysis, providing an overall assessment of the proposed observation strategy across the different orbital regimes.

4.3.1. Detected Passes

To assess the validity of the proposed observation strategy a two-weeks observation campaign is performed, starting on 1 January 2025, with optical telescopes working in the dark time. The efficiency of the strategy in covering the entire Field of Regard (FoR) was evaluated by comparing the number of detected objects with the total number of objects that entered the sensor FoR at least once during the respective time window.

To quantify the performance improvements achieved by the proposed multi-regime strategy, a comparison was conducted against a baseline static fixed-point survey, a standard observation mode to detect uncatalogued space objects. In this baseline configuration, all sensors in the network were set to a fixed Zenith pointing (0° Azimuth, 90° Elevation). This setup represents a standard staring surveillance mode where detection relies solely on the natural transit of objects through the sensor FoV. Table 4 summarizes the detection performance for both strategies across each orbital regime.

Table 4. Detection performance comparison between the proposed multi-regime observation strategy and a baseline fixed-point survey (0° Az, 90° El) during the two-week optical campaign. The table summarizes the total population, the number of objects entering the sensors FoR, and the number of unique objects detected at least once ($\geq$1) or at least three times ($\geq$3) for each orbital regime. Coverage percentages are calculated relative to the objects within the FoR.

Parameter	HLEO	MEO	GEO	Total
Population	3097	575	1424	5096
FoR objects	3096	575	1424	5095
Proposed Strategy				
$\geq$1 detection	3075 (99.32%)	575 (100%)	1423 (99.93%)	5073 (99.57%)
$\geq$3 detections	2988 (96.51%)	574 (99.83%)	1423 (99.93%)	4985 (97.84%)
Baseline (Fixed-Point)				
$\geq$1 detection	2648 (85.53%)	443 (77.04%)	1 (0.07%)	3092 (60.69%)
$\geq$3 detections	1301 (42.02%)	295 (51.30%)	0 (0.00%)	1596 (31.32%)

Analyzing the data in Table 4, the superiority of the proposed dynamic strategy is evident. While the static survey manages to detect a significant portion of the HLEO population (85.53%), primarily because their shorter orbital periods are more strongly affected by perturbations and because their highly inclined and eccentric orbits naturally cross the local zenith, it does not achieve comprehensive coverage. The gap widens when considering the robustness of the surveillance: for the $\geq$3 detections metric, which serves as a proxy for the revisit capability essential for orbit determination and catalog maintenance,

the static strategy coverage drops to just 42.02% for HLEO and 51.30% for MEO. In stark contrast, the proposed strategy maintains coverage rates above 96% for both metrics across these regimes.

Furthermore, the static strategy is almost entirely ineffective for the GEO regime (0.07% coverage), which is an expected outcome given that a Zenith-pointing sensor at mid-latitudes does not intersect the geostationary belt. The proposed strategy, with its dedicated equatorial fence, achieves near-full coverage (99.93%) of GEO objects. This comparison quantitatively demonstrates that while a simple staring strategy may yield a baseline set of detections, the dynamic updating of the phase-aware and equatorial fences is critical for achieving the high revisit rates and global regime coverage required for effective catalog maintenance.

Focusing on the detection performance, the sensor network performing the phase-aware and equatorial observation strategies demonstrates an almost complete detection coverage of objects across all orbital regimes. This result highlights the high effectiveness of the proposed observation sequence, which enables the coverage of a wide portion of the night sky. The phase-aware fence dynamically targets regions with favorable illumination conditions, while the equatorial fence ensures continuous monitoring of the visible GEO belt.

Figure 10 illustrates the distribution of the average number of detections per object as a function of key Keplerian parameters. Each map represents the density of detected passes within binned regions of the orbital parameter space, allowing a visual correlation between object detectability and orbital characteristics. The heat map of average detected passes per bin in the (a, e) plane reveals distinct regions of high detection activity. The first zone, between approximately 7000 and 10,000 km in semi-major axis, corresponds to the HLEO population. These objects exhibit eccentricities up to 10^{-2}, reflecting slightly elongated but still predominantly low-eccentricity orbits typical of upper LEO and elliptical transfer trajectories. A second prominent band appears between $a \simeq 11{,}500$ km and 17,500 km, associated with MEO satellites, particularly navigation constellations such as GNSS systems. The high detection rate in this region indicates favorable observation geometry and consistent illumination conditions for these nearly circular orbits. A third region of enhanced detections extends from $a \simeq 25{,}000$ km to 31,000 km, corresponding to high-MEO orbits, including transfer and disposal trajectories related to navigation and geosynchronous missions. Finally, the GEO belt appears as a concentrated and sharply defined feature near $a \simeq 42{,}164$ km with negligible eccentricity, representing the GEO population. The right panel presents the distribution of detections as a function of inclination and RAAN. The vertical bands of high detection density correspond to clusters of objects sharing similar inclinations—these are characteristic of common launch or operational planes (e.g., $i \approx 55$–65° for navigation constellations and $i \approx 0^\circ$ for GEO). The uniform coverage across a wide range of RAAN values demonstrates the global reach of the simulated sensor network. Conversely, for high-inclination orbits ($i > 70^\circ$), the number of detections decreases noticeably. This reduction is primarily attributed to unfavorable orbital phasing with respect to the sensor locations, which limits the temporal alignment between the orbital passes and the local night-time visibility windows. The seven optical stations, distributed across different longitudes (see Table 2), still ensure that objects are observed from multiple viewing geometries, minimizing temporal and spatial coverage gaps, which in turn enhance the cataloging capability of the sensor network. It is worth stressing that the very high percentage of detections and the extensive coverage achieved by the proposed multi-regime strategy result in an almost complete overlap between the population distribution and the detection maps. Consequently, a direct graphical overlay of the coverage areas on the population density plots would yield a saturated visualization

with little informative value, as the strategy leaves virtually no significant gaps across the primary orbital regimes. Overall, the detection maps confirm the effectiveness of the combined observation strategy in achieving nearly complete sky coverage. The phase-aware fence provides repeated opportunities for detection of high-altitude objects under favorable lighting conditions, while the equatorial fence ensures continuous surveillance of the GEO and MEO belts. The resulting distribution of detections across the orbital parameter space indicates that the implemented strategy successfully balances sensitivity and temporal coverage, yielding a high probability of detection across all major orbital regimes.

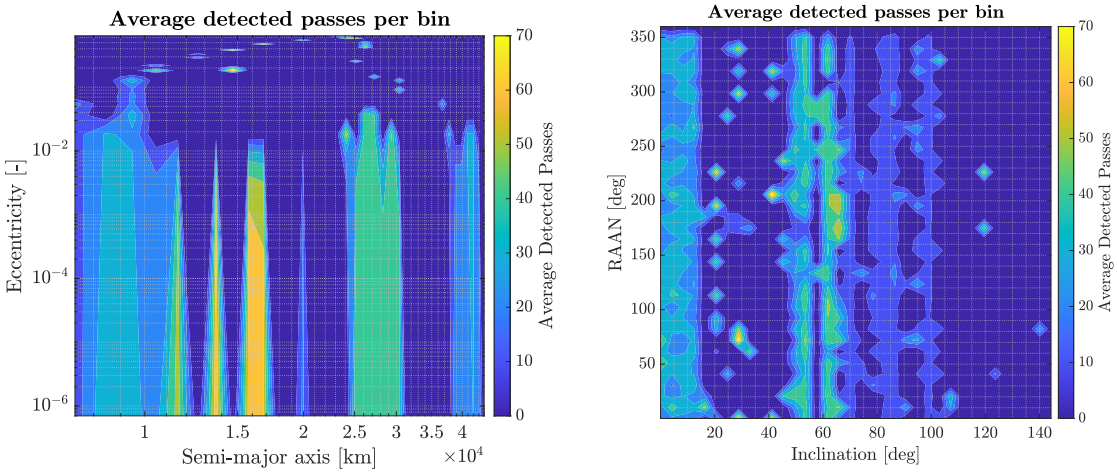

(**a**) Semi-major axis–eccentricity plane representation. (**b**) Inclination–RAAN plane representation.

Figure 10. Density distribution of objects detected passes as a function of Keplerian orbital parameters: (**a**) variation of density with semi-major axis (a) and eccentricity (e); (**b**) variation of density with inclination (i) and right ascension of the ascending node (RAAN or Ω).

To verify the capability of the network in monitoring small-scale debris, Figure 11 analyzes the relationship between the target RCS and the number of detected passes. The results demonstrate that the high sensitivity of the simulated optical sensors, combined with the optimized phase-aware strategy, allows for the effective detection of objects with RCS values lower than 0.1 m^2. A substantial number of passes is recorded even for targets in the 0.01–0.1 m^2 range, confirming that the observation strategy successfully exploits favorable phase angles to maximize the SNR. This capability ensures the visibility of faint objects that would otherwise fall below the detection threshold of standard static survey methods.

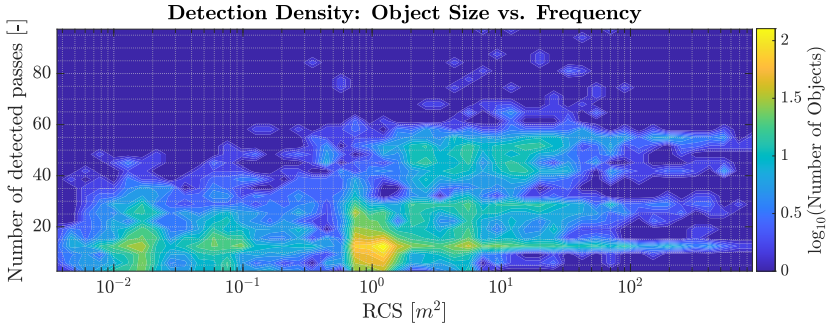

Figure 11. Detection density as a function of object size and frequency. The scatter plot highlights the system ability to detect small-cross-section objects (RCS $<$ 0.1 m^2) due to favorable illumination geometries.

To further substantiate the link between the observation strategy and cataloging performance, Figure 12 illustrates the cumulative distribution of the median time difference (Δt) between consecutive detected passes. This metric is crucial for orbit determination, as long gaps between observations lead to covariance growth and potential track loss. The distribution reveals that approximately 80% of the population has a median revisit time of one day or less, and nearly 95% of the objects are re-observed within a two-day window. Although a full long-term catalog maintenance simulation is not performed in this section due to the significant computational time required, this revisit frequency serves as an indicator of cataloging stability. The fact that the vast majority of the population is detected on a daily or bi-daily basis confirms that the strategy generates sufficient temporal density to support robust track-to-track association and orbit refinement.

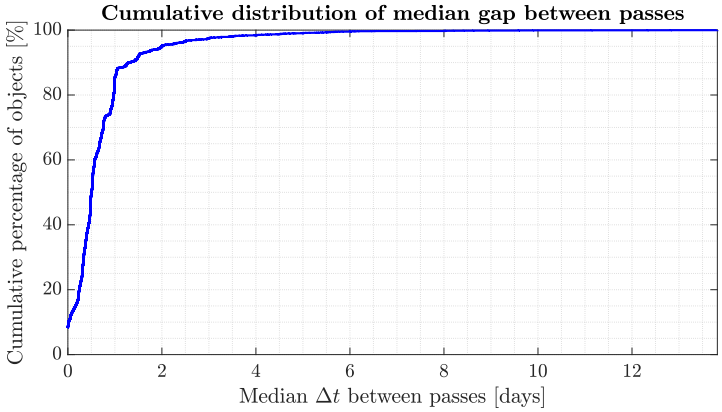

Figure 12. Cumulative distribution of the median time gap between consecutive detected passes for the entire simulated population. The curve highlights the high revisit rate achieved by the strategy.

Figure 13 presents the cumulative distribution of number of detected passes per object, separated by orbital regime. The data shown in the figure represent the number of passes of objects within the sensor FoR during which at least one detection was successfully recorded. This metric provides insight into the temporal sampling and coverage frequency achieved by the proposed observation strategy across different orbital populations. For the GEO population (red curve), a sharp increase is observed around 14 detected passes per object, which corresponds precisely to the number of nights in the two-week simulation. This behavior confirms that most GEO satellites are detected at least once per night, consistent with the continuous visibility of the geostationary belt from one of the seven globally distributed sensors. Since the same GEO object can enter the FoR of multiple sensors located at different longitudes, several objects show more than 14 detected passes, while a small fraction is not observed every night due to unfavorable illumination geometry, temporary exclusion from the FoR, or short interruptions in visibility. The MEO population (green curve) exhibits a smoother and broader distribution, with the majority of objects accumulating between 30 and 70 passes during the two-week period. This reflects the intermediate orbital periods (approximately 12 h) of navigation and medium-orbit satellites, which cross the same FoR multiple times per day. The equatorial fence strategy, optimized for continuous scanning of the equatorial region, effectively enables repeated detections of these objects, leading to a dense cumulative coverage. In contrast, the HLEO population (blue curve) is characterized by a gradual slope at lower detection numbers, indicating that a fraction of objects are observed only a few times during the campaign. Although HLEO satellites complete multiple orbital revolutions per day and thus cross the sensor FoR frequently, their high apparent angular velocity, the relative geometry, and limited illumination duration significantly reduce the effective number of successful detections. As a result, the cumulative curve saturates at a lower number of passes compared to MEO

and GEO, reflecting the intrinsically more challenging optical visibility conditions for this orbital regime.

Overall, also the cumulative distributions in Figure 13 highlight the strong performance of the combined phase-aware and equatorial observation strategies. GEO and MEO objects benefit from the continuous equatorial monitoring, while HLEO objects are efficiently captured through dynamic scanning near the Earth's shadow boundary. The resulting detection rates confirm that the observation strategy provides comprehensive temporal and spatial coverage across all major orbital regimes, ensuring reliable support for cataloging and orbit determination activities.

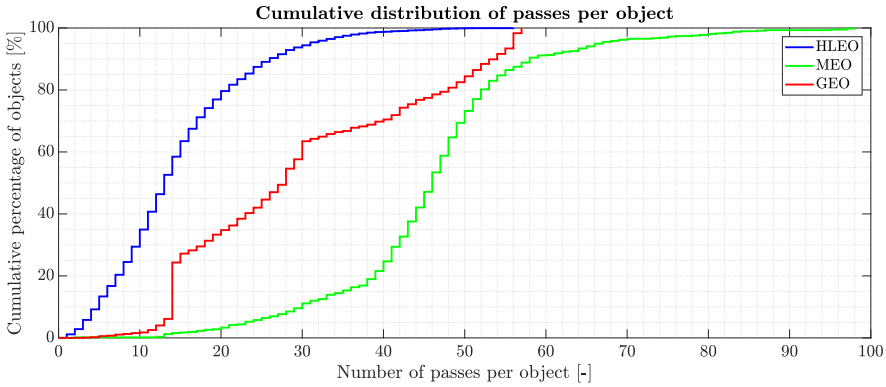

Figure 13. Cumulative distribution of the number of detected passes per object for each orbital population (HLEO, MEO, and GEO) during the two-week observation campaign. The cumulative percentage represents the fraction of objects that experienced up to a given number of detections within the pass inside the sensor FoR.

4.3.2. Track-to-Track and Cataloging

This section presents the results obtained by applying the track-to-track correlation method described in Section 3.2. The dataset used for this analysis spans a narrower, five-day observation window, in contrast to the two-week interval considered in the previous section. Optical observations of objects in the HLEO, MEO, and GEO regimes are analyzed. Only measurements acquired within 24 h of one another are included in the correlation process. Moreover, for each object in the population, all observation sets containing at least three measurements were deemed valid for analysis. This threshold corresponds to the minimum number of observations required to perform track compression, which is essential for extracting the corresponding attributable.

The results, summarized in Table 5, are expressed in terms of the number of cataloged, analyzed, and total objects, whose definitions are provided below for clarity:

- Total objects: The entire population of objects within each orbital regime, irrespective of the availability of multiple observations or correlation results.
- Analyzed objects: All objects observed within the selected time window that have at least two available tracks, separated by no more than 24 h. This represents the effective subset of the population eligible for correlation testing.
- Cataloged objects: Objects for which at least one positive correlation ($corr_{idx} < 1$) was identified within the complete set of analyzed tracks. These correspond to successfully linked observations belonging to the same object.
- Correlatable percentage: Number of analyzed objects with respect to the total number of objects.
- Correlated percentage: Number of cataloged objects with respect to the number of analyzed objects.

Table 5. Track-to-track correlation performance during the five-day sub-window of the optical campaign. The table summarizes the number of cataloged, analyzed, and total objects for each orbital regime.

Parameter	HLEO	MEO	GEO
Total number of objects	3096	575	1424
Number of analyzed objects	2599	575	1422
Number of cataloged objects	337	506	1400
Correlatable object percentage	2599/3096 → 83.95%	575/575 → 100.00%	1422/1424 → 99.86%
Correlated object percentage	337/2599 → 12.97%	506/575 → 88.00%	1400/1422 → 98.45%

The results indicate that the method performance for the MEO and GEO regimes is significantly more robust than for the HLEO one. This difference can be attributed to two closely related factors: the temporal distribution of the measurements and the underlying assumptions of the track-to-track correlation method. Specifically, the TBI approach assumes purely Keplerian motion and does not account for perturbative accelerations. Consequently, for the HLEO regime, being the most dynamically perturbed among the three, the method accuracy degrades as the observation time-span increases. Indeed, the presence of unmodeled dynamics introduces discrepancies that hinder convergence toward the correct correlation solution. Therefore, the validity of this approach for HLEO objects is inherently limited to relatively short time intervals.

This behavior can be more clearly appreciated in Figure 14, which presents the cumulative sum of the correct association number as a function of the time difference between tracks for the three regimes considered. The figure provides a direct visualization of how the temporal separation between tracks influences the algorithm ability to correctly associate measurements belonging to the same object. It can be observed that, across all three regimes, the highest number of successful correlations occurs when the time interval between tracks is shorter than one hour. This result is particularly remarkable for HLEO and MEO, and is consistent with the expected behavior of the method, since shorter time separations correspond to smaller orbital deviations, which facilitate convergence toward the correct correlation solution.

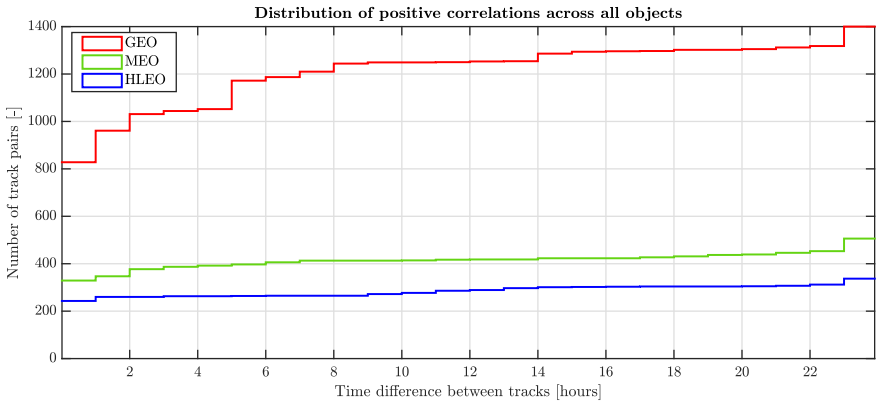

Figure 14. Cumulative distribution of the number of correctly associated track pairs for each orbital population (HLEO, MEO, and GEO) during the five-day observation campaign.

For GEO objects, once the one-hour threshold is exceeded, and up to separations of approximately 24 h, there is an almost twofold increase in the number of correct associations. This behavior reflects the relatively stable dynamical environment of this regime, where perturbation effects induce only minor deviations over short to medium timescales. As a

result, even when the temporal gap between tracks extends to several hours, the assumption of near-Keplerian motion remains valid, allowing the correlation method to maintain good performance.

For MEO objects, the improvement in the number of correct associations with increasing time separation is more limited. Beyond approximately four hours, the cumulative number of correct associations tends to plateau. This is indicative of the intermediate dynamical nature of the MEO region, where perturbations become more significant compared to GEO but are still less dominant than in highly elliptical orbits. Consequently, the validity of the pure Keplerian approximation used in the correlation algorithm begins to degrade at shorter timescales than in the previous case.

For HLEO objects, on the other hand, the number of correct associations remains almost constant once the time difference between observation tracks exceeds approximately two hours. This behavior highlights the strong sensitivity of HLEO to unmodeled perturbations over short timescales. In such conditions, the Keplerian assumption underlying the track-to-track correlation method becomes increasingly inadequate as the propagation interval grows, leading to a sharp reduction in correlation success. Nonetheless, it is worth pointing out that HLEO performance can be improved by extending the analysis time window. Overall, the analysis demonstrates the feasibility of building up a comprehensive space objects catalog with the proposed sensor network.

5. Conclusions

SST remains a critical component of space operations, supporting collision avoidance, space object monitoring, and the long-term sustainability of orbital environments. This study presents and evaluates an advanced composite observation strategy that integrates a phase-aware fence with an equatorial fence, implemented within the enhanced SΞNSIT simulation framework. Nightly campaign simulations demonstrate that this dual-mode approach effectively covers multiple orbital regimes, achieving detection rates exceeding 99% over a two-week period. Furthermore, the strategy ensures a high revisit frequency, with most objects observed multiple times (more than three detectable passes) within the simulation window, thereby enhancing catalog stability. The results demonstrate that the correlation method performance is strongly dependent on the orbital regime and, in particular, on the characteristic timescale over which the Keplerian approximation remains valid. Results also confirm that for regimes with weaker perturbations, such as GEO, reliable correlations can be achieved even with track separations of several hours, whereas for highly perturbed regimes like HLEO, the temporal validity of the method is considerably more restricted.

While a comprehensive sensitivity analysis of the observation strategy settings was not performed due to the high computational cost of large-scale simulations, future work could address this limitation by defining an objective function to be minimized. Such an approach would enable the identification of optimal or near-optimal ranges for key observation parameters (e.g., exposure time and projection altitude) while also providing insight into their fault tolerance. Moreover, the track-to-track correlation method could be further improved by accounting for the dominant perturbations in the relevant orbital regime. For objects in HLEO, the J_2 perturbation is the main contributor to short-term orbital evolution. Including J_2 in the model would reduce the impact of unmodeled dynamics, enhancing orbit propagation accuracy and improving correlation performance, particularly when the time separation between tracks is significant.

These enhancements will contribute to a more resilient and accurate SST architecture, which is essential for safeguarding both current and future space activities.

Author Contributions: Conceptualization, A.M., S.S.R. and A.D.R.; methodology, A.M., S.S.R. and A.D.R.; software, A.M., S.S.R. and A.D.R.; validation, A.M., S.S.R., A.D.R. and M.F.M.; formal analysis, A.M., S.S.R. and A.D.R.; investigation, A.M., S.S.R. and A.D.R.; resources, M.F.M.; data curation, A.M., S.S.R. and A.D.R.; writing—original draft preparation, A.M., S.S.R. and A.D.R.; writing—review and editing, M.F.M. and A.M.; visualization, A.M., S.S.R. and A.D.R.; supervision, M.F.M.; project administration, M.F.M.; funding acquisition, M.F.M. All authors have read and agreed to the published version of the manuscript.

Funding: This research has received funding as part of the work developed for the agreement n. 2023-37-HH.0 for the project "Attività tecnico-scientifiche di supporto a C-SSA/ISOC e simulazione di architetture di sensori per SST", established between the Italian Space Agency (ASI) and Politecnico di Milano (POLIMI)—Project Identification Code (CUP) F43C23000130005.

Data Availability Statement: The raw data supporting the conclusions of this article will be made available by the authors on request.

Acknowledgments: The authors would like to express their gratitude to Leonardo S.p.A. (through its Electronics Division) for supporting the project within which the research activity.

Conflicts of Interest: The authors declare no conflicts of interest.

Abbreviations

The following abbreviations are used in this manuscript:

ECI	Earth Centered Inertial
FoR	Field of Regard
FoV	Field of View
GEO	Geostationary Orbit
HLEO	High-altitude Low Earth Orbit
IOD	Initial Orbit Determination
LEO	Low Earth Orbit
MEO	Medium Earth Orbit
RAAN	Right Ascension of the Ascending Node
RCS	Radar Cross Section
ROD	Refined Orbit Determination
RSO	Resident Space Object
SMD	Squared Mahalanobis Distance
SNR	Signal-to-Noise Ratio
SSA	Space Situational Awareness
SSN	Space Surveillance Network
SST	Space Surveillance and Tracking
SΞNSIT	Space Surveillance Sensor Network Simulation Tool
TBI	Two-Body Integrals
TLE	Two-Line Element
UT	Unscented Transform

References

1. Romano, M.; Carletti, T.; Daquin, J. The resident space objects network: A complex system approach for shaping space sustainability. *J. Astronaut. Sci.* **2024**, *71*, 31. [CrossRef]
2. European Space Agency. *ESA's Annual Space Environment Report*; Issue/Revision 9.1; European Space Agency: Paris, France, 2025. Available online: https://www.sdo.esoc.esa.int/publications/Space_Environment_Report_I9R1_20251021.pdf (accessed on 3 November 2025).
3. Choi, E.J.; Cho, S.; Lee, D.J.; Kim, S.; Jo, J.H. A study on re-entry predictions of uncontrolled space objects for space situational awareness. *J. Astron. Space Sci.* **2017**, *34*, 289–302. [CrossRef]
4. Patera, R.P. General method for calculating satellite collision probability. *J. Guid. Control Dyn.* **2001**, *24*, 716–722. [CrossRef]

5. Chatters, M.E.P.; Crothers, M.B.J. Chapter 19—Space Surveillance Network. In *AU-18 Space Primer*; Air University Press: Montgomery, AL, USA, 2009; pp. 249–258.
6. Flohrer, T.; Krag, H. Space surveillance and tracking in ESA's SSA programme. In Proceedings of the 7th European Conference on Space Debris, Darmstadt, Germany, 18–21 April 2017; Volume 7.
7. European Union Space Surveillance and Tracking. *EUSST Service Portfolio*; European Union Space Surveillance and Tracking: Madrid, Spain, 2023. Available online: https://www.eusst.eu/sites/default/files/documents/EUSST_Service_Portfolio.pdf (accessed on 21 August 2025).
8. Delmas, F.; Perez, C.; Nunes, P. Future evolutions of EUSST collision avoidance service. *J. Space Saf. Eng.* **2024**, *11*, 133–142. [CrossRef]
9. Bonaccorsi, S.; Montaruli, M.F.; Di Lizia, P.; Peroni, M.; Panico, A.; Rigamonti, M.; Del Prete, F. Conjunction analysis software suite for space surveillance and tracking. *Aerospace* **2024**, *11*, 122. [CrossRef]
10. Montaruli, M.F.; Di Lizia, P.; Cordelli, E.; Ma, H.; Siminski, J. A stochastic approach to detect fragmentation epoch from a single fragment orbit determination. *Adv. Space Res.* **2023**, *72*, 3713–3733. [CrossRef]
11. Grattagliano, P.; Mignocchi, A.; Montaruli, M.F.; Di Lizia, P.; Di Cecco, A.; Castronuovo, M.M. Early stage characterization of on-orbit fragmentation events. *Acta Astronaut.* **2025**, *236*, 32–46. [CrossRef]
12. Montaruli, M.F.; Facchini, L.; Faraco, N.; Di Lizia, P.; Massari, M.; Bianchi, G.; Bortolotti, C.; Maccaferri, A.; Roma, M.; Peroni, M.; et al. Third Long-March 5B Re-Entry Campaign through Italian Space Surveillance Radars. *Adv. Space Res.* **2025**, *75*, 2139–2155. [CrossRef]
13. Pardini, C.; Anselmo, L. Impact of the time span selected to calibrate the ballistic parameter on spacecraft re-entry predictions. *Adv. Space Res.* **2008**, *41*, 1100–1114. [CrossRef]
14. Pardini, C.; Anselmo, L. Assessing the risk and the uncertainty affecting the uncontrolled re-entry of manmade space objects. *J. Space Saf. Eng.* **2018**, *5*, 46–62. [CrossRef]
15. Faucher, P.; Peldszus, R.; Gravier, A. Operational space surveillance and tracking in Europe. *J. Space Saf. Eng.* **2020**, *7*, 420–425. [CrossRef]
16. Montaruli, M.F.; Purpura, G.; Cipollone, R.; De Vittori, A.; Facchini, L.; Di Lizia, P.; Massari, M.; Peroni, M.; Panico, A.; Cecchini, A.; et al. An orbit determination software suite for Space Surveillance and Tracking applications. *CEAS Space J.* **2024**, *16*, 619–633. [CrossRef]
17. Hussain, K.F.; Thangavel, K.; Gardi, A.; Sabatini, R. Autonomous optical sensing for space-based space surveillance. In Proceedings of the 2023 IEEE Aerospace Conference, Big Sky, MT, USA, 4–11 March 2023; pp. 1–9. [CrossRef]
18. Rizzuto, S.S.; Cipollone, R.; De Vittori, A.; Di Lizia, P.; Massari, M. Object detection on space-based optical images leveraging machine learning techniques. *Neural Comput. Appl.* **2025**. [CrossRef]
19. Maruskin, J.M.; Scheeres, D.J.; Alfriend, K.T. Correlation of optical observations of objects in Earth orbit. *J. Guid. Control Dyn.* **2009**, *32*, 194–209. [CrossRef]
20. Laurin, D.G.; Beraldin, J.A.; Blais, F.; Rioux, M.; Cournoyer, L. Three-dimensional tracking and imaging laser scanner for space operations. In *Laser Radar Technology and Applications IV, Proceedings of the Volume 3707, AEROSENSE '99, Orlando, FL, USA, 5–9 April 1999*; SPIE Digital Library: Bellingham, WA, USA, 1999; pp. 278–289. [CrossRef]
21. Cordelli, E.; Vananti, A.; Schildknecht, T. Analysis of laser ranges and angular measurements data fusion for space debris orbit determination. *Adv. Space Res.* **2020**, *65*, 419–434. [CrossRef]
22. Montaruli, M.F.; De Luca, M.A.; Massari, M.; Bianchi, G.; Magro, A. Operational Angular Track Reconstruction in Space Surveillance Radars through an Adaptive Beamforming Approach. *Aerospace* **2024**, *11*, 451. [CrossRef]
23. Montaruli, M.F. Radar Initial Orbit Determination Method from Angular Track and Doppler Shift Measurements. *Astrodynamics* **2025**, *9*, 993–1013. [CrossRef]
24. Cataldo, D.; Gentile, L.; Ghio, S.; Giusti, E.; Tomei, S.; Martorella, M. Multibistatic radar for space surveillance and tracking. *IEEE Aerosp. Electron. Syst. Mag.* **2020**, *35*, 14–30. [CrossRef]
25. Warner, J.G.; Carbott, G.; Ward, E.M.; Lemm, K. Comparing radius of convergence in solving the nonlinear least squares problem for precision orbit determination of geodetic satellites. In Proceedings of the AIAA/AAS Astrodynamics Specialist Conference, Long Beach, CA, USA, 13–16 September 2016; p. 5339. [CrossRef]
26. Working Group on Covariance Realism. Covariance and Uncertainty Realism in Space Surveillance and Tracking. 2016. Available online: https://apps.dtic.mil/sti/pdfs/AD1020892.pdf (accessed on 7 January 2026).
27. Gooding, R.H. A new procedure for the solution of the classical problem of minimal orbit determination from three lines of sight. *Celest. Mech. Dyn. Astron.* **1996**, *66*, 387–423. [CrossRef]
28. Armellin, R.; Di Lizia, P. Probabilistic optical and radar initial orbit determination. *J. Guid. Control Dyn.* **2018**, *41*, 101–118. [CrossRef]
29. Pastor, A.; Sanjurjo-Rivo, M.; Escobar, D. Initial orbit determination methods for track-to-track association. *Adv. Space Res.* **2021**, *68*, 2677–2694. [CrossRef]

30. Fujimoto, K.; Scheeres, D.J. Correlation of optical observations of Earth-orbiting objects and initial orbit determination. *J. Guid. Control Dyn.* **2012**, *35*, 208–221. [CrossRef]
31. Little, B.D.; Frueh, C. Space situational awareness sensor tasking: Comparison of machine learning with classical optimization methods. *J. Guid. Control Dyn.* **2020**, *43*, 262–273. [CrossRef]
32. Caceres, K.; Moreno, D.; García, F.A.; Anton, A.; Ghita, M.; Bivolaru, M.; Stelmecke, D.; Richard, P.; Carbognani, A.; Zubowicz, T.; et al. How will COPLA work within EU SST? In Proceedings of the 73rd International Astronautical Congress (IAC), Paris, France, 18–22 September 2022.
33. Schubert, M.; Kebschull, C.; Gelhaus, J.; Silvestri, S. Evaluating sensor tasking strategies for object cataloging in GEO. *Acta Astronaut.* **2025**, *228*, 7–16. [CrossRef]
34. Rowland, J.; McKnight, D.; Pino, B.P.; Reihs, B.; Stevenson, M.A. A worldwide network of radars for space domain awareness in low earth orbit. In Proceedings of the Advanced Maui Optical and Space Surveillance Technologies Conference (AMOS), Maui, HI, USA, 14–17 September 2021.
35. Purpura, G.; De Vittori, A.; Cipollone, R.; Di Lizia, P.; Massari, M.; Colombo, C.; Di Cecco, A.; Salotti, L. SΞNSIT: A software suite for observation scheduling and performance assessment of SST sensor networks. In Proceedings of the 72nd International Astronautical Congress (IAC), Dubai, United Arab Emirates, 25–29 October 2021; International Astronautical Federation: Dubai, United Arab Emirates, 2021; pp. 1–13.
36. Acton, C.; Bachman, N.; Semenov, B.; Wright, E. SPICE tools supporting planetary remote sensing. *Int. Arch. Photogramm. Remote Sens. Spat. Inf. Sci.* **2016**, *41*, 357–359. [CrossRef]
37. Acciarini, G.; Baydin, A.G.; Izzo, D. Closing the gap between SGP4 and high-precision propagation via differentiable programming. *Acta Astronaut.* **2025**, *226*, 694–701. [CrossRef]
38. Acton, C.; Bachman, N.; Semenov, B.; Wright, E. A look towards the future in the handling of space science mission geometry. *Planet. Space Sci.* **2018**, *150*, 9–12. [CrossRef]
39. Purpura, G.; De Vittori, A.; Cipollone, R.; Facchini, L.; Di Lizia, P.; Massari, M.; Di Cecco, A.; Salotti, L. GA-based optimal tasking for SST sensor networks in the SENSIT tool. In Proceedings of the International Astronautical Congress (IAC), Paris, France, 18–22 September 2022; pp. 1–10.
40. Fortin, F.A.; De Rainville, F.M.; Gardner, M.A.; Parizeau, M.; Gagné, C. DEAP: Evolutionary algorithms made easy. *J. Mach. Learn. Res.* **2012**, *13*, 2171–2175. [CrossRef]
41. Cibin, L.; Chiarini, M.; Pellegrini, R.; Bernardi, F.; Dimare, L.; Cicalò, S.; Perozzi, E. SUTED—A detailed study for the application of the Flyeye Telescope to the survey of the MEO orbital region. In Proceedings of the 8th European Conference on Space Debris, Darmstadt, Germany, 20–23 April 2021; p. 70.
42. Flohrer, T.; Krag, H.; Klinkrad, H.; Schildknecht, T. Feasibility of performing space surveillance tasks with a proposed space-based optical architecture. *Adv. Space Res.* **2011**, *47*, 1029–1042. [CrossRef]
43. Srivastava, V.K.; Ashutosh, A.; Roopa, M.V.; Ramakrishna, B.N.; Pitchaimani, M.; Chandrasekhar, B.S. Spherical and oblate Earth conical shadow models for LEO satellites: Applications and comparisons with real time data and STK to IRS satellites. *Aerosp. Sci. Technol.* **2014**, *33*, 135–144. [CrossRef]
44. Zhang, R.; Tu, R.; Zhang, P.; Liu, J.; Lu, X. Study of satellite shadow function model considering the overlapping parts of Earth shadow and Moon shadow and its application to GPS satellite orbit determination. *Adv. Space Res.* **2019**, *63*, 2912–2929. [CrossRef]
45. Srivastava, V.K.; Pitchaimani, M.; Chandrasekhar, B.S. Eclipse prediction methods for LEO satellites with cylindrical and cone geometries: A comparative study of ECSM and ESCM to IRS satellites. *Astron. Comput.* **2013**, *2*, 11–17. [CrossRef]
46. Montenbruck, O.; Gill, E.; Lutze, F.H. Satellite orbits: Models, methods, and applications. *Appl. Mech. Rev.* **2002**, *55*, B27–B28. [CrossRef]
47. Gisolfi, L.; Rossi, A.; Marzari, F. A refined space environment index for the characterization of in-orbit fragmentations. *Aerospace* **2025**, *12*, 483. [CrossRef]
48. Qiu, T.; Wang, Y.; Hong, J.; Xing, K.; Du, S.; Mu, J. An in-orbit measurement method for elevation antenna pattern of MEO synthetic aperture radar based on nano calibration satellite. *Remote Sens.* **2022**, *14*, 741. [CrossRef]
49. Milani, A.; Sansaturio, M.E.; Chesley, S.R. The asteroid identification problem IV: Attributions. *Icarus* **2001**, *151*, 150–159. [CrossRef]
50. Gronchi, G.F.; Dimare, L.; Milani, A. Orbit determination with the two-body integrals. *Celest. Mech. Dyn. Astron.* **2010**, *107*, 299–318. [CrossRef]
51. Gronchi, G.F.; Farnocchia, D.; Dimare, L. Orbit determination with the two-body integrals. II. *Celest. Mech. Dyn. Astron.* **2011**, *110*, 257–270. [CrossRef]
52. Gronchi, G.F.; Bau, G.; Maro, S. Orbit determination with the two-body integrals: III. *Celest. Mech. Dyn. Astron.* **2015**, *123*, 105–122. [CrossRef]
53. Dichter, M.J.; Wojcik, J.J. Characterizing the convergence behavior of Gauss's method of initial orbit determination. *J. Guid. Control Dyn.* **2020**, *43*, 998–1002. [CrossRef]

54. Ghorbani, H. Mahalanobis distance and its application for detecting multivariate outliers. *Facta Univ. Ser. Math. Inform.* **2019**, *34*, 583–595. [CrossRef]
55. 18th Space Defense Squadron. Space-Mission-Related Data from Space-Track.org. Available online: https://www.space-track.org/ (accessed on 15 April 2025).

Disclaimer/Publisher's Note: The statements, opinions and data contained in all publications are solely those of the individual author(s) and contributor(s) and not of MDPI and/or the editor(s). MDPI and/or the editor(s) disclaim responsibility for any injury to people or property resulting from any ideas, methods, instructions or products referred to in the content.